This is the accepted manuscript made available via CHORUS. The article has been
published as:

One- and two-neutron removal cross sections of ^{24}O

D. A. Divaratne, C. R. Brune, H. N. Attanayake, T. Baumann, D. Bazin, A. Gade, S. M.
Grimes, P. M. King, M. Thoennessen, and J. A. Tostevin

Phys. Rev. C **98**, 024306 — Published 13 August 2018
DOI: 10.1103/PhysRevC.98.024306

One- and Two-Neutron Removal Cross Sections of ^{24}O

D. A. Divaratne,[1,2] C. R. Brune,[1] H. N. Attanayake,[1] T. Baumann,[3] D. Bazin,[3]
A. Gade,[3,4] S. M. Grimes,[1] P. M. King,[1] M. Thoennessen,[3,4] and J. A. Tostevin[5]

[1] *Department of Physics and Astronomy, Ohio University, Athens, OH 45701, USA*
[2] *Department of Physics, Miami University, Oxford, OH 45056, USA*
[3] *National Superconducting Cyclotron Laboratory, Michigan State University, East Lansing, Michigan 48824, USA*
[4] *Department of Physics and Astronomy, Michigan State University, East Lansing, Michigan 48824, USA*
[5] *Department of Physics, Faculty of Engineering and Physical Sciences,*
University of Surrey, Guildford, Surrey GU2 7XH, United Kingdom

(Dated: July 24, 2018)

Cross sections of one- and two-neutron removal reactions of ^{24}O, leading to the ^{23}O($\frac{1}{2}^+$) ground state and to bound final states of ^{22}O, have been measured at the National Superconducting Cyclotron Laboratory. The experiment was conducted using the S800 spectrograph and a ^{24}O beam energy of 92.3 MeV/u. The measured ^{23}O ground state and ^{22}O inclusive cross section values, of 74(11) mb and 146(33) mb, respectively, are in good agreement with calculations using eikonal reaction dynamics and shell-model nuclear structure overlaps. The widths at half maximum of the associated parallel momentum distributions of these cross sections, deduced from Gaussian fits, are 115(13) MeV/c for ^{23}O and 309(36) MeV/c for ^{22}O in the projectile rest frame. The data and calculations strongly support the shell-model description of ^{24}O as a spherical, doubly-magic structure.

I. INTRODUCTION

One- and two-nucleon removal experiments with fast, secondary beams play an important role in understanding the single-particle structure of rare nuclei. They offer a high-luminosity technique, alternative to traditional light-ion induced transfer reactions, able to track the evolution of the shell structure and the spectroscopic strengths of valence nucleons in the most rare isotopes [1, 2]. The removal reaction technique is very well suited to fast, low intensity rare isotope beams produced using projectile fragmentation [3], due to its relatively large cross sections and the very high experimental detection efficiency of the reaction residues.

Removal reaction events are identified by detection of the fast reaction residues which travel forwards in the laboratory with a velocity close to that of the projectile beam. Coincidence measurements are often made with the decay gamma-rays from events in which the residual nucleus is populated in particle bound excited states, when these exist. The dependence of one- and two-nucleon removal cross sections and their momentum distributions on the strengths (spectroscopic factors C^2S and two-nucleon amplitudes) and quantum numbers (primarily the orbital angular momenta ℓ) of the orbitals, j^π, from which the nucleon(s) are removed, e.g. [2, 4], can be used to determine the active valence nucleon configurations in the ground state wave function of the projectile. In general, the cross sections for producing such hole-like states, which also leave reaction products in excited states, are significant. So, final-state-exclusive measurements allow one to probe the strengths (and occupancies) and ℓ-values of the removed nucleon(s) from the magnitudes and the widths of the parallel momentum distributions of the cross sections of residues in the projectile rest frame, respectively.

The magnitudes of the measured cross sections probe directly the one- and two-nucleon overlaps of the projectile ground state with the populated final states of the residues. So, comparisons with reaction theory calculations using overlaps from many-body theory alow single- or two-nucleon configurations can be explored in short-lived rare isotopes. The proton-magic chain of oxygen isotopes is of particular interest since shell evolution is at play and nuclear properties have been measured even in the neutron continuum beyond the neutron dripline [5]. Furthermore, theoretical configuration-interaction shell-model approaches, both with [6, 7] and without the continuum [5, 8, 9], mean field methods [10], and ab-initio-type many-body approaches based on chiral forces [11–18] have been using the oxygen isotopes as a demanding test-bed for the inclusion of the many drivers of structural change that make ^{24}O doubly-magic [19–21] and the heaviest bound $Z = 8$ isotope. The most recent experimental investigations included studies of the matter radii [22] and two-neutron decay properties of excited unbound states [23].

In this article, we report inclusive one- and two-neutron removal cross sections and their parallel momentum distributions from ^{9}Be-induced removal reactions on a ^{24}O projectile beam at 92 MeV/u, complementing related carbon-target data taken at 920 MeV/u [24] and from proton-induced reactions at 62 MeV/u [25, 26].

II. EXPERIMENT

The experiment was conducted at the National Superconducting Cyclotron Laboratory (NSCL) at Michigan State University using the high resolution S800 spectrograph [27]. A 92.3-MeV/u secondary beam of ^{24}O with a 1% momentum spread was produced and selected with the A1900 fragment separator [28] using a ^{48}Ca primary beam of 140 MeV/u impinging on a ^{9}Be production target with a thickness of 1034 mg/cm^2. The rare-isotope beam was transported to the S800 where the secondary neutron removal reactions occurred in a 188-mg/cm^2-thick ^{9}Be reaction target located at the target position of the spectrograph. The rare-isotope projectile beam impinging onto the target was characterized using two plastic timing scintillators. One was placed at the exit of the A1900 fragment separator and the other at the object of the S800 spectrograph, approximately 30 m apart. These detectors yield time-of-flight information as well as the incoming beam intensity and transmission efficiency.

The secondary beam of interest contained ^{24}O and ^{27}Ne. The measured rate of ^{24}O transmitted to the experimental end station was 0.25 pps/pnA with a ^{24}O purity of 46%. The time-of-flight spectrum of the incoming secondary beam was obtained by calibrating the flight times between the two scintillators upstream of the target. The magnetic rigidity and the energy of ^{24}O and ^{27}Ne were calculated using the LISE++ program [29] along with their velocities, 12.51 cm/ns and 13.63 cm/ns, respectively. This information, together with the distance between the two timing detectors in cm, was utilized to calibrate the time of flight in ns. Fig. 1 shows the time-of-flight spectrum from the A1900 to object scintillator, characterizing the incoming beam composition. The Full Width at Half Maximum (FWHM) of the time-of-flight peaks are observed to be about 1%, which comes from momentum spread of the ^{24}O and ^{27}Ne nuclei exiting the A1900 separator due to its momentum acceptance.

The projectile-like neutron-removal residues were identified and characterized with the spectrograph. The focal plane of the S800 is equipped with two cathode readout drift chambers (CRDCs) for x-y position determination of the beam, an ionization chamber for energy-loss measurements, and a plastic scintillator [30] that served as trigger and time-of-flight reference relative to two plastic beam line scintillators.

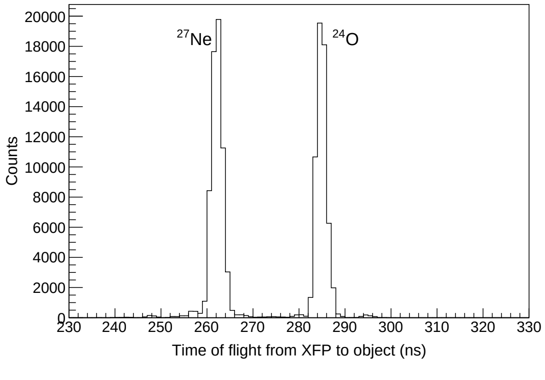

FIG. 1. The calibrated time-of-flight spectrum from A1900 timing detector (XFP) to object scintillator (before the reaction target).

The oxygen isotope identification is shown in the Fig. 2, where the S800 magnets were set for the magnetic rigidity of ^{23}O with the energy loss in the reaction target taken into account. Plotted is the calibrated energy loss in the S800 ionization chamber versus the time of flight between the object scintillator (the fast timing scintillator which is located just before the S800 magnets) and the trigger scintillator in the S800 focal plane. This spectrum was calibrated using runs with unreacted ^{24}O and ^{27}Ne beam and took into account the position-dependent light travel time in the scintillator to the photomultiplier tubes. The Ref. [27] provides more details on how the calibration is performed. The ^{23}O can cleanly be identified in the spectrum. Figure 3 shows the same correlation for the experimental runs with the S800 magnets on the ^{22}O setting with its magnetic rigidity and energy loss taken into consideration. In both cases, the ^{24}O incoming beam was chosen with a software gate on the time-of-flight spectrum shown in Fig. 1.

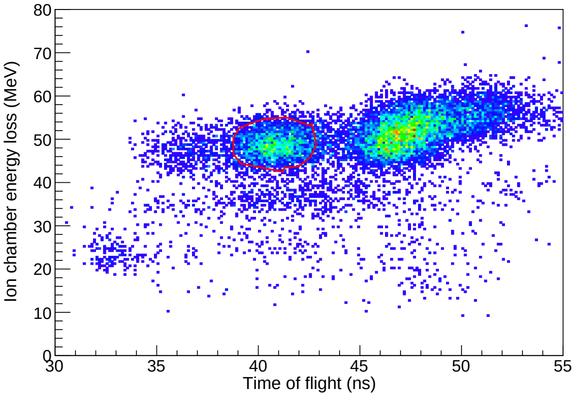

FIG. 2. The ion chamber energy loss versus time-of-flight spectrum from the object scintillator to the trigger scintillator after applying the ^{24}O gate for combined production runs with the ^{23}O setting. The red outline shows the applied ^{23}O contour gate used for cross section calculations.

III. DETERMINATION OF THE NEUTRON REMOVAL CROSS SECTIONS

The inclusive cross sections for the nucleon removal reactions to all bound final states was determined from the yield of the detected projectile-like reaction residues divided by the number of incoming ^{24}O projectiles relative to the number density of the ^{9}Be knockout target. For the normalization of the incoming beam intensity via scaler values, so-called unreacted runs were taken where the magnetic rigidity of the S800 spectrograph was set to accept ^{24}O passing through the target. The ^{23}O cross section is

$$\sigma = \frac{^{23}\text{O particles}}{C_{obj} \times P \times t \times \tau \times \epsilon}, \tag{1}$$

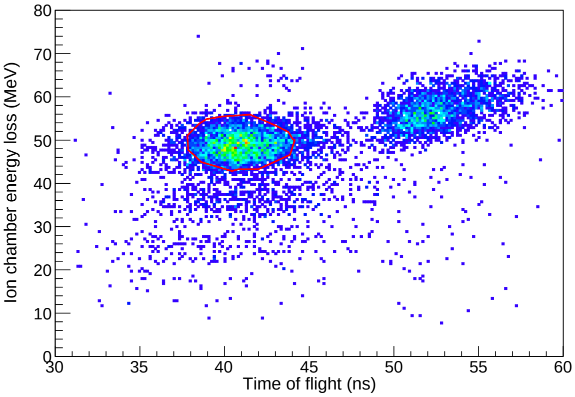

FIG. 3. The ion chamber energy loss versus time-of-flight spectrum from the object scintillator to the trigger scintillator for the ^{22}O setting. The red outline shows the applied ^{22}O contour gate used for cross section calculations.

where C_{obj} is the scaler for object scintillator, P is the number of incident ^{24}O per scaler count, t is the thickness of the reaction target, τ is the ratio between the live trigger scalers and raw trigger scalers, and ϵ is the total efficiency of CRDCs and scintillators. The incoming ^{24}O per scaler count was obtained from the unreacted beam runs. The ^{22}O cross section was determined using the same procedure. Both CRDCs and beam line scintillators have a calculated efficiency of almost 100%.

The systematic uncertainty from possible backgrounds and the choice of oxygen-isotope identification gate (see Figs. 2 and 3) is estimated to be 9%. The systematic uncertainties in the one- and two-neutron knockout momentum acceptance are estimated to be 10% and 20%, respectively, and are due to the possible loss of acceptance relative to 100% efficiency. This esimate is based on simulations similar to those described in [31]. Finally, systematic uncertainties of 5% from beam purity and stability and 2% from the reaction target thickness provided by the target manufacturer were considered. All the systematic uncertainties were added in quadrature to the statistical uncertainty to obtain the total error for the cross sections. The measured neutron knockout cross section values for ^{23}O and ^{22}O are 74(11) and 146(33) mb, respectively.

IV. DETERMINATION OF THE WIDTHS OF THE MOMENTUM DISTRIBUTIONS

The position information from the two CRDCs in the S800 focal plane in conjunction with the optics code COSY [32] were used to reconstruct the parallel momentum distribution of the nucleon removal residues on an event-by-event basis. The extracted parallel momentum distributions of the unreacted ^{24}O, and the ^{23}O, and ^{22}O residues, in the projectile rest frame, are shown in Figs. 4-6. The experimental resolution was modeled as the convolution of rectangular and Gaussian distributions, with the parameters determined from a fit to the distribution measured for the unreacted ^{24}O beam. The FWHM of the resolution function determined in this manner is 99(11) MeV/c.

The measured ^{23}O and ^{22}O distributions were fitted with Gaussian forms of unknown width convoluted with the resolution function. The parallel momentum distributions are not exactly Gaussian in shape, having a tail on the low momentum side. This experimental asymmetry, the result of modest transfers of energy to the target in both the elastic breakup and inelastic removal events (involving target excitation), which are neglected in the eikonal model theoretical description, can be reproduced when including these effects [33, 34].

The fitted results are shown in Figs. 5 and 6. For ^{23}O, the fitted momentum range -100 MeV/c to 200 MeV/c was chosen to avoid the low-momentum tail of the distribution, leading to a FWHM of 115(13) MeV/c for the intrinsic ^{23}O parallel momentum distribution. For ^{22}O, the range -100 MeV/c to 400 MeV/c was fitted leading to a FWHM of 309(36) MeV/c for the ^{22}O inclusive parallel momentum distribution.

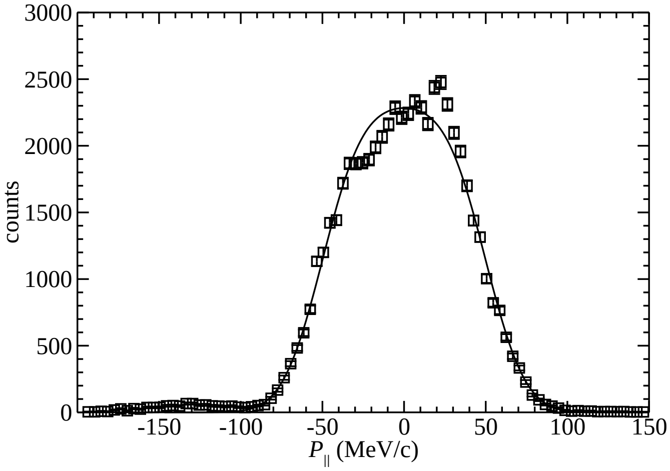

FIG. 4. The measured parallel momentum distribution of unreacted ^{24}O in the projectile rest frame (points). The solid curve is the result of the fit described in Sec. IV.

V. REACTIONS ANALYSIS

We adopt the eikonal model approaches of Refs. [2, 35] to compute the fast one- and two-neutron removal reaction yields from the ^{24}O(0^+) projectile ground state at 92.3 MeV/u. Here, fast refers to intermediate energy reactions in which the interaction/removal timescale is typical of a direct reaction. For the 92.3 MeV/u ^{24}O beam, with $v/c{\approx}0.41$, the interaction time is therefore $\approx 8d\times10^{-24}$ s, where d, in fm, is the (short) strong interaction path length in the surface-grazing collisions that

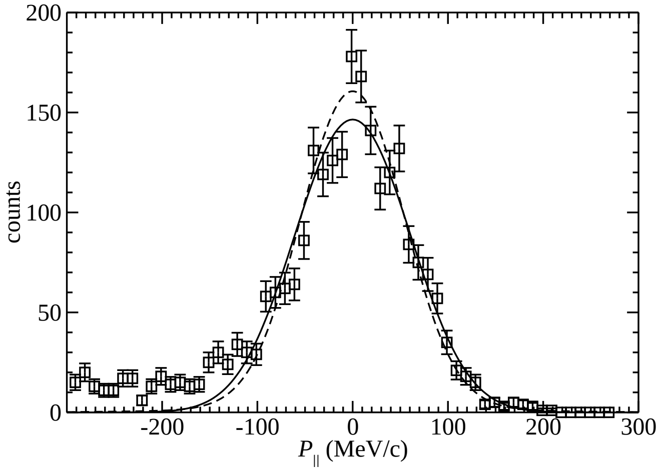

FIG. 5. The measured parallel momentum distribution of the ^{23}O reaction residues in the projectile rest frame (points). The solid curve is the result of the fit described in Sec. IV and the dashed curve is a theoretical prediction described in Sec. V.

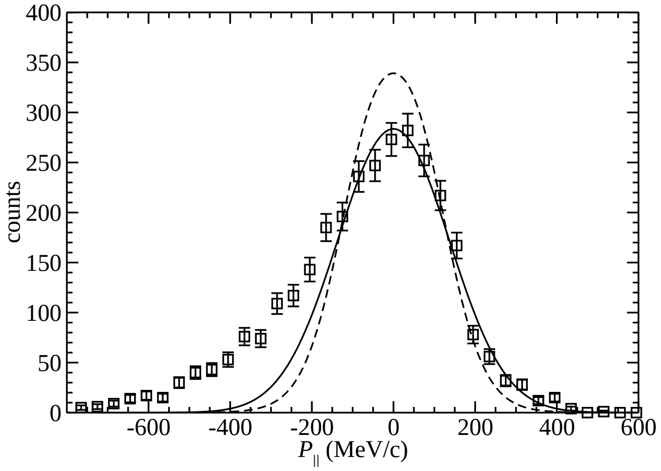

FIG. 6. The measured parallel momentum distribution of the ^{22}O reaction residues in the projectile rest frame (points). The solid curve is the result of the fit described in Sec. IV. The dashed curve is a theoretical prediction, described in Sec. V, after convolution with the experimental resolution.

dominate the removal mechanism. Those nuclear reaction and structure parameter choices relating to nuclear size were constrained using the procedures detailed in Ref. [4]. The direct reaction pathways to ^{22,23}O and the sequential pathways to ^{22}O, the latter through intermediate, neutron-unbound ^{23}O excited states, are represented schematically in Fig. 7 together with their Q values and the thresholds for neutron emission from ^{23}O and ^{22}O [36]. The most important ^{23}O final states for the present analysis, the $1/2^+$ ground state and the (just) neutron-unbound excited $5/2^+$ state at 2.78(11) MeV [37] are shown. Other experimental and shell-model states are discussed in more detail below.

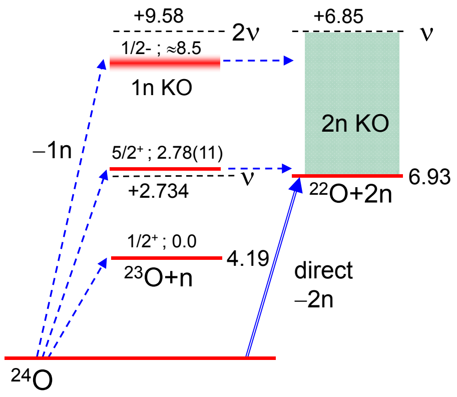

FIG. 7. (Color online) Direct and indirect reaction pathways calculated in the one- and two-neutron removal reactions of ^{24}O to ^{22,23}O. The relevant one- and two-neutron thresholds are indicated by the dashed horizontal lines, labeled as ν and 2ν, respectively, from Ref. [36]. The ^{23}O $1/2^-$ unbound-state position shown is that given by the HF calculation.

The theoretical direct one-neutron removal partial cross section to a given final state of the $(A-1)$-body residual nucleus, $^{23}\mathrm{O}(j^\pi)$, at excitation energy E^* is [2]

$$\sigma_{\rm th} = \left(\frac{A}{A-1}\right)^N C^2S(\ell j^\pi)\,\sigma_{\rm sp}(n\ell j,S_n^*)\;, \tag{2}$$

where C^2S is the shell-model spectroscopic factor. The first factor is the A-dependent center-of-mass correction term, where N is the number of oscillator quanta of the major shell of the removed nucleon; this is $N=2$ for the sd-shell orbitals of interest here. The single-particle cross section $\sigma_{\rm sp}$, for the removal of a neutron with quantum numbers $n\ell j$ and an effective separation energy S_n^* $(= S_n(\mathrm{g.s.})+E^*)$, is calculated using a normalized neutron single-particle overlap, i.e. unit spectroscopic strength. The ^{24}O ground-state neutron separation energy is $S_n(\mathrm{g.s.})$=4.192 MeV [36]. These single-particle cross sections $\sigma_{\rm sp}$ include the contributions from both the elastic and inelastic breakup mechanisms with the ^{9}Be target. Details of these two incoherent contributions can be found e.g. in Ref. [1] and references therein, and experimental tests, that confirm that the model calculations correctly reproduce their relative magnitudes, can be found in Refs. [38] and [39] - and in Ref. [40] for the case of the two-nucleon removal reaction.

We will denote the root mean squared (rms) radius of the ^{23}O core nucleus by R_c and that of the single-particle orbital of the removed neutron by R_{sp}. Within the reaction model, the primary sensitivity of the calculated single-particle cross sections σ_{sp} is to these radial extents that requires a consistent choice of these two sizes [4]. These radii dictate the reaction geometry: (i) via the residual nucleus density, that determines the range of its highly-absorptive optical potential with the target nucleus, and (ii) via the resulting probability density of the wave function of the removed nucleon at and near the projectile surface. For physically reasonable ranges of these radii, the σ_{sp} change linearly with both R_{sp} [4] and R_c [31].

Calculations of the $\sigma_{\rm sp}$ require the (eikonal) neutron-target and residue-target elastic scattering S-matrices. These are calculated using the static density limit of the Glauber multiple scattering series, e.g. [41]. The absorptive neutron- and ^{23}O-target interactions, from which the S-matrices are calculated, thus use the single-folding $t_{NN}\rho_t$ model (nucleon) and double-folding $t_{NN}\rho_r\,\rho_t$ model (residue, r). The inputs needed are the point neutron and proton one-body densities of the residue and target (t) nuclei and an effective nucleon-nucleon (NN) interaction t_{NN}.

The n and p one-body densities of the reaction residues are computed using spherical Hartree-Fock (HF) calculations with the Skyrme SkX interaction [42]. Such calculations have been shown to provide a very good global description of the root mean squared (rms) sizes [43] and radial forms of the matter and charge distributions [44] of both stable and asymmetric nuclei. In the present case, the computed ^{23}O and ^{22}O HF densities have matter rms radii of 2.93 fm and 2.86 fm, respectively. These values are consistent with the radii deduced (assuming Fermi-form densities) from the analysis of the 900 MeV/u ^{23}O and ^{22}O interaction cross section measurements on a carbon target, of Ref. [45].

The same density is used for all ^{23}O final states and is adequate for calculation of the highly-absorptive ion-ion S-matrix for the limited range of impact parameters needed for the fast grazing collisions that are involved. The nucleon density of the ^{9}Be target is taken to be of Gaussian form with a point-nucleon root-mean-squared radius of 2.36 fm. A Gaussian NN effective interaction [46] is used with strength calculated from the free neutron-neutron and neutron-proton total cross sections at the projectile incident energy/nucleon and with the ratio of the real-to-imaginary parts of the NN forward-scattering amplitudes (α_{pp} and α_{np}) taken from the tabulated values (at 100 MeV) obtained in the nucleon-nucleus multiple-scattering analysis of Ray [47].

We construct the required bound neutron single-particle wave functions (overlaps) in ^{24}O as the eigenstates of Woods-Saxon potentials with radius and diffuseness parameters ($r_0, a_0 = 0.7$ fm). We include a spin-orbit potential with the same geometry parameters, r_0, a_0, and a fixed strength of $V_{\rm so} = 6.0$ MeV. The r_0 values for the neutron sd-shell orbitals are constrained by a spherical HF calculation for ^{24}O (see [4] for details). These values are $r_0 = 1.0184$ fm ($2s_{1/2}$) and $r_0 = 1.1735$ fm ($1d_{5/2}$). The binding potential depths for these single-particle orbitals are adjusted to reproduce the S_n^* value appropriate for each final state.

The shell-model spectroscopic factors, using the USD-B effective interaction [48], and theoretical one-neutron removal partial cross sections are shown in Table I. Using instead shell-model calculations with the SDPF-M effective interaction [49], produces very similar outcomes, with $C^2S(1/2^+) = 1.769$ and $C^2S(5/2^+) = 5.593$, as tabulated in [24]. The experimental cross sections are also shown in Table I.

TABLE I. Final states and shell-model spectroscopic factors for the single-neutron removal reactions from ^{24}O. The table shows the theoretical partial $1n$-removal cross sections for the transitions to the bound and unbound ^{23}O(j^π) final states. The $1n$-removal spectroscopic factors are from USD-B interaction shell-model calculations [48]. The calculated inclusive direct $2n$-removal cross section to bound shell-model states of ^{22}O, taken from Table II, and the calculated and experimental inclusive cross sections to ^{22}O are also shown.

$E^*(^{23}$O) (MeV)	j^π	C^2S	$\sigma_{\rm sp}$ (mb)	$\sigma_{\rm th}$ (mb)	$\sigma_{\rm exp}$ (mb)
0.00	$1/2^+$	1.810	36.20	69.7	74(11)
2.78	$5/2^+$	5.665	19.43	118.3	
Direct	$-2n$			29.9	
Inclusive	^{22}O			148.2	146(33)

The sensitivity of the σ_{sp} to R_{sp} (via the bound-state potential parameters) and to R_c have been studied for systems of different masses, e.g. [2, 4, 31, 50, 51]. Here, the sensitivity of the ^{24}O ground-state to ^{23}O($1/2^+$) ground-state σ_{sp} to deviations from the R_{sp}, of the HF-constrained binding potential, and R_c values is

$$\frac{\delta\sigma_{sp}}{\sigma_{sp}} = 3.23\frac{\delta R_{sp}}{R_{sp}} - 1.65\frac{\delta R_c}{R_c}. \tag{3}$$

The variations for the other states are similar. The signs of the two terms here reflect the primary importance to the removal reaction mechanism of that part of the neutron single-particle orbital that extends radially beyond the core nucleus.

Calculations of the parallel momentum distributions of the ^{23}O residues, using the same bound states and elastic S-matrix inputs as above, use the formalism of Ref. [52]. The predicted ^{23}O ground state momentum distribution is in reasonable agreement with the data, after convolution with the experimental resolution, as shown in Fig. 5. The predicted distribution is slightly narrower than that found experimentally: the predicted FWHM is 89 MeV/c versus 115(13) MeV/c obtained from fitting the experimental data with a Gaussian distribution. For the $5/2^+$ state, the ^{23}O residue has been determined to be neutron unbound, by 45(2) keV [37] with respect to the first neutron threshold of 2.734 MeV [36], and will decay to ^{22}O+n. This small continuum energy results in a negligible additional recoil broadening of the resulting ^{22}O momentum distribution from that of ^{23}O. This recoil, that requires folding the calculated ^{23}O distribution with a rectangular distribution of total width 18 MeV/c, is neglected.

The ^{23}O final states above and in Figure 7 are the dominant shell-model and experimentally observed states with hole-like strength. Other, particle-like states (resonances) at 4.0 and 5.3 MeV have been identified via the neutron-adding (d,p) reaction [53], proposed to be $(3/2^+)$ and pf-shell intruder configurations, respectively. In addition to the strong $1/2^+$ and $5/2^+$ states presented above and in Figure 7, which together account for 7.48 units of single-particle strength, the USD-B shell model calculation also predicts several weak fragments of j^π (C^2S) strength to states near the ^{23}O two-neutron threshold. In detail, the shell model predicts additional $1/2^+$ (0.133), $5/2^+$ (0.086) and $3/2^+$ (0.045) overlaps to unbound states at excitation energies between 7 and 9 MeV, with σ_{sp} of 16.0, 14.3 and 13.0 mb, respectively. In addition, there is a weak $3/2^+$ (0.090) overlap with a state at 4.0 MeV, with a σ_{sp} of 16.2 mb. We note that this fragment coincides with the $(3/2^+)$ resonance reported from the ^{22}O(d,p) data set [53]. Collectively, these fragments add further indirect pathways and predict an additional cross section of 5.9 mb for population of bound ^{22}O residues and, together with the major $1/2^+$ and $5/2^+$ states, account for 7.83 of the 8 available units of sd-shell neutron single-particle strength. The remaining 0.17 units are distributed among multiple fragments lying above the ^{23}O two-neutron threshold of 9.58 MeV.

The possibility also arises of a contribution to the ^{22}O inclusive cross section due to removal reaction strength from neutrons occupying the more-well-bound $1p_{1/2}$ orbital. The HF calculations for ^{24,23}O, referred to above, bind the $1p_{1/2}$ orbital ≈8.5 MeV more strongly than the $2s_{1/2}$ orbital, suggesting a likelihood of $1/2^-$ removal strength to unbound ^{23}O* final states with a continuum energy ≈5.8 MeV – and lying below the second neutron decay threshold from ^{23}O. The binding potential radius parameter for this p-wave orbital is $r_0 = 1.244$ fm and the calculated single particle cross section is 12.4 mb. So, dependent upon the actual position and the fragmentation of this $1/2^-$ hole strength, the measured ^{22}O cross section may contain a contribution from this source of 12.4 mb per single particle unit. In the absence of further knowledge, the HF $1/2^-$ state position is represented in Figure 7. We note that any $1/2^-$ contribution of this magnitude lies within the uncertainty on the measured ^{22}O inclusive cross section shown in Table I. Furthermore, the calculated ^{22}O momentum distribution from such a cross section component, after accounting for the additional recoil broadening due to the decay of this ^{23}O$(1/2^-)$ continuum state, is essentially identical to that of the (just unbound) $5/2^+$ state and such a component would not affect the shape of the theoretical ^{22}O inclusive parallel momentum distribution.

The several bound shell-model final states of the ^{22}O residue (with threshold $S_n = 6.85$ MeV [36]) will also be populated by the direct two-neutron removal process. These smaller contributions are calculated using the generalization of the eikonal model approach for the $2n$-removal reaction as developed in Refs. [35, 54], the shell-model two-nucleon amplitudes (TNAs), and the neutron bound state radius parameters r_0 discussed above. The definition of the shell-model TNA and the phase conventions of the single particle states are detailed in Ref. [54]. The two-neutron separation energy from ^{24}O is S_{2n}(g.s.)=6.926 MeV and the two removed nucleons are each assumed to be bound by the average separation energy $\bar{S}^*_n = [S_{2n}(\text{g.s.})+E^*]/2$ for each final state. The additional inputs needed, the ^{22}O-target optical potential and its elastic S-matrix, are computed as discussed above, based on the spherical HF density for ^{22}O. These calculated direct $2n$-removal partial cross sections are included in Table II.

There are presently no data that isolate such direct $2n$-removal cross section components, and hence no systematics or comparisons of calculated and measured cross sections, in cases where the two nucleons are relatively weakly-bound - here S_{2n}(g.s.)= 6.93 MeV. For reactions involving more well-bound nucleon pairs, see e.g. Fig. 2 of Ref. [35], where the two-nucleon S_{2N}(g.s) range from 26–34 MeV, the measured direct cross sections are smaller than the theoretical values, with $R_s(2N) = \sigma_{\text{exp}}/\sigma_{\text{th}}(-2N) \approx 0.5$. Here, the full calculated inclusive value has been added to the theoretical ^{22}O production cross section in Table I. That is, we assume $R_s(2n) = 1$. The direct $2n$-removal partial parallel momentum distributions for the ^{22}O residue final states were calculated using the eikonal model formalism of Ref. [55].

TABLE II. Theoretical direct two-neutron removal reaction cross sections, $\sigma_{\text{th}}(-2n)$, from ^{24}O. Tabulated are the cross sections to all predicted ^{22}O(J^π, E^*) shell-model final states below the first neutron threshold of 6.85 MeV [36]. These cross sections are calculated using the shell-model TNA from the USD-B interaction [48] and the sd-model space.

$E^*(^{22}$O) (MeV)	J^π	$\sigma_{\text{th}}(-2n)$ (mb)
0.000	0^+	3.71
3.158	2^+	8.48
4.762	0^+	1.09
4.795	3^+	5.33
6.363	2^+	4.16
6.734	4^+	7.12
Inclusive	$-2n$	29.88

The predicted inclusive momentum distribution for ^{22}O is now compared to the data, by weighting the calculated ^{23}O(5/2+) unbound state and direct $2n$-removal distributions by their theoretical cross sections and convoluting their sum with the experimental resolution. This prediction, shown as the dashed curve in Fig. 6, is seen to be slightly narrower than the fit to the measured distribution of Section. IV.

VI. DISCUSSION AND CONCLUSIONS

We have measured fast one- and two-neutron removal reactions of ^{24}O, incident on a ^{9}Be target at 92.3 MeV/u, and carried out a consistent comparison of these new data with eikonal reaction model plus shell-model structure calculations for the direct and indirect pathways to the ^{23}O and ^{22}O final states, shown schematically in Fig.7. As was shown in Table I, the calculated cross sections are in very good agreement with the measurements. The experimental to theoretical cross sections ratio, $R_s = \sigma_{\rm exp}/\sigma_{\rm th}$, from the values in Table I for the ^{23}O ground state, is $R_s = 1.06(15)$, where the error estimate includes only experimental uncertainties. The associated value of ΔS [4], based on the ^{24}O neutron and proton separation energies of the 2016 atomic mass evaluation (AME) [36] is $\Delta S = -21.3$ MeV. These values are also consistent with the removal reaction systematics for neutron-rich nuclei on ^{9}Be and/or ^{12}C target nuclei; as presented in Refs. [4, 56, 57].

A related one-neutron removal measurement, on a carbon target, was conducted at GSI [24] with a beam energy of 920 MeV/u. They reported only the one-neutron removal cross section to bound ^{23}O, and deduced a value for $C^2S(1/2^+) = 1.74(19)$, in good agreement with the SDPF-M and USD-B shell-model spectroscopic factors. We note however that that analysis assumed a smaller value of the ^{24}O neutron separation energy, i.e. 3.61 MeV, of the 2003 AME [58], whereas the most recent value is 4.19(20) MeV [36]. The present $1/2^+$-state cross section is increased by 11% if the earlier (smaller) S_n value is used. More recent experiments, of ^{24}O on a proton target at 62 MeV/u, were also conducted at RIKEN [25, 26]. The inelastic proton scattering of ^{24}O showed evidence for an $N = 16$ spherical shell closure, based on the measured β_2 and $E(2_1^+)$ systematics along the oxygen isotopic chain [25]. The cross section and momentum distribution following proton-induced neutron knockout to the unbound ^{23}O first excited state, identified using the measured ^{22}O and neutron four-momenta, confirmed this state as $5/2^+$ with a large spectroscopic factor [26]. The deduced $C^2S(5/2^+)$ was 4.1(4) based on a distorted waves impulse approximation analysis of that alternative reaction mechanism. Our ^{23}O and ^{22}O channel data sets are fully consistent with the large – filled $1/2^+$ and $5/2^+$ sub-shells – shell-model spectroscopic factors and two-neutron amplitudes and provide strong additional support for the presence of a good spherical shell closure at $N = 16$ in ^{24}O and for its doubly-magic character.

ACKNOWLEDGMENTS

We acknowledge the contributions of A. Schiller to the early phases of this project. This work was supported in part by the U.S. Department of Energy under grant number DE-FG02-88ER40387 and by the National Science Foundation under Grant No. PHY-1102511 and PHY-1565546. The support of the United Kingdom Science and Technology Facilities Council (STFC) Research Grants ST/F005314/1 and ST/L005743/1 (for JAT) is also acknowledged.

---

[1] J. A. Tostevin, Nucl. Phys. **A682**, 320c (2001).
[2] P. G. Hansen and J. A. Tostevin, Annu. Rev. Nucl. Part. Sci. **53**, 219 (2003).
[3] A. Gade *et al.*, Prog. in Part. and Nucl. Phys **60**, 161 (2008).
[4] A. Gade *et al.*, Phys. Rev. C **77**, 044306 (2008).
[5] B. A. Brown, Int. J. Mod. Phys. E **26**, 1740003 (2017).
[6] A. Volya, and V. Zelevinsky, Phys. Atomic Nuclei **77**, 969 (2014).
[7] K. Fossez, and J. Rotureau, N. Michel, W. Nazarewicz, Phys. Rev. C **96**, 024308 (2017).
[8] B. Alex Brown *et al.*, Phys. Rev. C **72**, 057301 (2005).
[9] T. Otsuka *et al.*, Phys. Rev. Lett. **105**, 032501 (2010).
[10] J. J. Li, J. Margueron, W. H. Long, and N. Van Giai, Phys. Lett. **B753**, 97 (2016).
[11] S. Binder, P. Piecuch, A. Calci, J. Langhammer, P. Navratil, and R. Roth, Phys. Rev. C **88**, 054319 (2013).
[12] S. K. Bogner, H. Hergert, J. D. Holt, A. Schwenk, S. Binder, A. Calci, J. Langhammer, and R. Roth, Phys. Rev. Lett. **113**, 142501 (2014).
[13] G. R. Jansen, J. Engel, G. Hagen, P. Navratil, and A. Signoracci, Phys. Rev. Lett. **113**, 142502 (2014).
[14] K. Hagino, and H. Sagawa, Phys. Rev. C **89**, 014331 (2014).
[15] A. Cipollone, C. Barbieri, and P. Navratil, Phys. Rev. C **92**, 014306 (2015).
[16] A. Ekstrom et al., Phys. Rev. C **91**, 051301 (2015).
[17] J. Simonis, K. Hebeler, J. D. Holt, J. Menendez, and A. Schwenk, Phys. Rev. C **93**, 011302 (2016).
[18] J. Simonis, S. R. Stroberg, K. Hebeler, J. D. Holt, and A. Schwenk, Phys. Rev. C **96**, 014303 (2017).
[19] A. Ozawa *et al.*, Phys. Rev. Lett. **84**, 5493 (2000).
[20] M. Stanoiu *et al.*, Phys. Rev. C **69**, 034312 (2004).
[21] C. R. Hoffman *et al.*, Phys. Lett. **B672**, 17 (2009).
[22] V. Lapoux, V. Soma, C. Barbieri, H. Hergert, J. D. Holt, and S. R. Stroberg, Phys. Rev. Lett. **117**, 052501 (2016).
[23] M. D. Jones *et al.*, Phys. Rev. C **92**, 051306 (2015).
[24] R. Kanungo *et al.*, Phys. Rev. Lett. **102**, 152501 (2009).
[25] K. Tshoo *et al.*, Few-Body Systems **54**, 459 (2013).
[26] K. Tshoo *et al.*, Phys. Lett. **B739**, 19 (2014).
[27] D. Bazin *et al.*, Nucl. Instrum. Methods Phys. Res., Sect. B **204**, 629 (2003).
[28] D. J. Morrissey *et al.*, Nucl. Instrum. Methods Phys. Res., Sect. B **204**, 90 (2003).
[29] O. B. Tarasov and D. Bazin, Nucl. Instrum. Methods Phys. Res., Sect. B **266**, 4657 (2008).
[30] J. Yurkon *et al.*, Nucl. Instrum. Methods Phys. Res., Sect. A **422**, 291 (1999).
[31] G. F. Grinyer *et al.*, Phys. Rev. C **86**, 024315 (2012).
[32] K. Makino and M. Berz, Nucl. Instrum. Methods Phys. Res., Sect. A **558**, 346 (2006).
[33] J. A. Tostevin *et al.*, Phys. Rev. C **66**, 024607 (2002).
[34] R. Stroberg *et al.*, Phys. Rev. C **90**, 034301 (2014).
[35] J. A. Tostevin and B. A. Brown, Phys. Rev. C **74**, 064604 (2006).

[36] W.J. Huang, G. Audi, Meng Wang, F.G. Kondev, S. Naimi and Xing Xu, Chinese Physics C **41**, 030002 (2017); 030003 (2017).

[37] A. Schiller *et al.*, Phys. Rev. Lett. **99**, 112501 (2007).

[38] D. Bazin, R. J. Charity, M. A. Famiano, 1 A. Gade, V. Henzl, D. Henzlova, S. Hudan, H. C. Lee, S. Lukyanov, W. G. Lynch, S. McDaniel, M. Mocko, A. Obertelli, A. M. Rogers, L. G. Sobotka, R. T. de Souza, J. R. Terry, J. A. Tostevin, M. B. Tsang, and M. S. Wallace, Phys. Rev. Lett. **102**, 232501 (2009).

[39] K. Wimmer, D. Bazin, A. Gade, J. A. Tostevin, T. Baugher, Z. Chajecki, D. Coupland, M. A. Famiano, T. K. Ghosh, G. F. Grinyer, R. Hodges, M.E. Howard, M. Kilburn, W. G. Lynch, B. Manning, K. Meierbachtol, P. Quarterman, A. Ratkiewicz, A. Sanetullaev, S. R. Stroberg, M. B. Tsang, D. Weisshaar, J. Winkelbauer, R. Winkler, M. Youngs, Phys. Rev. C **90**, 064615 (2014).

[40] K. Wimmer, D. Bazin, A. Gade, J.A. Tostevin, T. Baugher, Z. Chajecki, D. Coupland, M.A. Famiano, T. Ghosh, G.F. Grinyer, R. Hodges, M.E. Howard, M. Kilburn, W.G. Lynch, B. Manning, K. Meierbachtol, P. Quarterman, A. Ratkiewicz, A. Sanetullaev, S.R. Stroberg, M.B. Tsang, D. Weisshaar, J. Winkelbauer, R. Winkler, M. Youngs, Phys. Rev. C **85**, 051603(R) (2012).

[41] J. S. Al-Khalili, J. A. Tostevin, and I. J. Thompson, Phys. Rev. C **54**, 1843 (1996).

[42] B. A. Brown, Phys. Rev. C **58**, 220 (1998).

[43] B. A. Brown, S. Typel, and W. A. Richter, Phys. Rev. C **65**, 014612 (2002).

[44] W. A. Richter and B. A. Brown, Phys. Rev. C **67**, 034317 (2003).

[45] R. Kanungo *et al.*, Phys. Rev. C **84**, 061304(R) (2011).

[46] J. A. Tostevin, J. Phys. G: Nucl. Part. Phys. **25**, 735 (1999).

[47] L. Ray, Phys. Rev. C **20**, 1857 (1979).

[48] B. A. Brown and W. A. Richter, Phys. Rev. C **74**, 034315 (2006).

[49] Y. Utsuno, T. Otsuka, T. Mizusaki, and M. Honma, Phys. Rev. C **60**, 054315 (1999).

[50] A. Gade *et al.*, Phys. Rev. C **69**, 034311 (2004).

[51] A. Gade *et al.*, Phys. Rev. Lett. **93**, 042501 (2004).

[52] C. A. Bertulani and P. G. Hansen, Phys. Rev. C **70**, 034609 (2004).

[53] Z. Elekes *et al.*, Phys. Rev. Lett. **98**, 102502 (2007).

[54] J. A. Tostevin, G. Podolyák, B. A. Brown and P. G. Hansen, Phys. Rev. C **70**, 064602 (2004).

[55] E. C. Simpson, J. A. Tostevin, D. Bazin, and A. Gade, Phys. Rev. C **79**, 064621 (2009).

[56] J. A. Tostevin, Prog. Theor. Phys. Suppl. **196**, 275 (2012).

[57] J. A. Tostevin and A. Gade, Phys. Rev. C **90**, 047602 (2014).

[58] G. Audi *et al.*, Nucl. Phys. **A729**, 337 (2003).